ORIGINAL ARTICLE

Image-based biomarkers for engineering neuroblastoma patient-specific computational models

Silvia Hervas-Raluy[1] · Diego Sainz-DeMena[1] · Maria Jose Gomez-Benito[1] · Jose Manuel García-Aznar[1]

Abstract

Childhood cancer is a devastating disease that requires continued research and improved treatment options to increase survival rates and quality of life for those affected. The response to cancer treatment can vary significantly among patients, highlighting the need for a deeper understanding of the underlying mechanisms involved in tumour growth and recovery to improve diagnostic and treatment strategies. Patient-specific models have emerged as a promising alternative to tackle the challenges in tumour mechanics through individualised simulation. In this study, we present a methodology to develop subject-specific tumour models, which incorporate the initial distribution of cell density, tumour vasculature, and tumour geometry obtained from clinical MRI imaging data. Tumour mechanics is simulated through the Finite Element method, coupling the dynamics of tumour growth and remodelling and the mechano-transport of oxygen and chemotherapy. These models enable a new application of tumour mechanics, namely predicting changes in tumour size and shape resulting from chemotherapeutic interventions for individual patients. Although the specific context of application in this work is neuroblastoma, the proposed methodologies can be extended to other solid tumours. Given the difficulty for treating paediatric solid tumours like neuroblastoma, this work includes two patients with different prognosis, who received chemotherapy treatment. The results obtained from the simulation are compared with the actual tumour size and shape from patients. Overall, the simulations provided clinically useful information to evaluate the effectiveness of the chemotherapy treatment in each case. These results suggest that the biomechanical model could be a valuable tool for personalised medicine in solid tumours.

Keywords Computational oncology · Imaging biomarkers · Neuroblastoma · Patient-specific modelling · Finite element method

1 Introduction

Cancer is the second most common cause of death among children aged 1–14 years in the United States, surpassed only by accidents [1]. Globally, approximately 400,000 children are diagnosed with cancer each year [2]. One in every six children diagnosed with cancer in the US does not survive beyond 5 years. Over the past 50 years, there has been significant improvement in the prognosis for children and adolescents diagnosed with cancer. In the mid-1970s, only 58% of children (ages 0–14 years) with cancer survived

for at least 5 years. By 2011–2017, this rate increased to 84.7% [1]. However, despite this progress, the development of new drugs exclusively for childhood cancer has been limited. People who have had cancer during childhood or adolescence need follow-up care and enhanced medical surveillance for the rest of their lives because of the risk of complications related to the disease or its treatment that can last for, or arise, many years after they complete treatment for their cancer. Health issues that manifest months or years after treatment has ended are commonly referred to as late effects.

Among children, one of the most common types of cancer is neuroblastoma [3]. Neuroblastoma is a type of cancer that is highly representative of the cancer disease itself, since it is strongly heterogeneous with very diverse clinical courses that may vary from an indolent disease causing little or no harm and exhibiting spontaneous regression, to an aggressive disease with fatal progression [4]. For these reasons,

✉ Jose Manuel García-Aznar
  jmgaraz@unizar.es

1 Multiscale in Mechanical and Biological Engineering (M2BE), Dpt. of Mechanical Engineering, Aragon Institute of Engineering Research (I3A), University of Zaragoza, Zaragoza, Spain

neuroblastoma is considered a paradigm of cancer disease and an excellent context of application for the validation of novel developments which have the ambition to be of potential application in a large variety of cancers.

The majority of current medical diagnostic practices result in imprecise approximations of treatment outcomes, often based on clinical trial results. However, since these results are based on averages, they might not be directly applicable to individual patients. Computational models have become an essential tool in the field of biomedical research, particularly in the study of complex diseases such as cancer [5–15]. These models allow researchers to simulate and analyse the behaviour of biological systems at different levels of complexity, from the molecular to the cellular levels [16, 17]. One of the key advantages of computational models is their versatility, which allows them to be applied to a wide range of biological questions and to different types of data, including genomic, proteomic, and imaging data. Patient-specific computational models are particularly important in the context of cancer research, as they may have the potential to improve the accuracy and effectiveness of cancer diagnosis, prognosis, and treatment. By integrating patient-specific data, including genetic information, imaging data, and clinical information, these models can provide more accurate predictions of disease progression and response to treatment. Furthermore, patient-specific models can be used to identify optimal treatment strategies for individual patients, potentially reducing the risk of adverse effects and improving treatment efficacy. Overall, the development of subject-specific computational models holds great promise for improving the diagnosis, treatment, and management of cancer, and represents a crucial area of research for the future of cancer care.

In this work, we hypothesise that the use of a computational model that predicts the outcome of the tumour during chemotherapy treatment could be used to identify when the treatment is going to return a positive response that would maximise the survival. To test this hypothesis, we developed a novel computational model of the neuroblastoma evolution that links cell processes with cancer growth and remodelling. The model is validated with two different patients classified at diagnosis as low and intermediate risk [18]. After applying a three-month chemotherapy treatment, the computational model is able to replicate the very different outcomes. It is imperative to emphasise the significance of developing models for the paediatric population, as this can potentially reduce the number of required clinical tests. However, the limited availability of data for model development and validation poses a significant challenge.

Despite the challenges associated with the availability of data, the presented computational model serves as a promising step towards improving the understanding and treatment of paediatric cancers. It is hoped that continued efforts

in this field will lead to the development of more accurate and effective models, ultimately benefiting the paediatric population.

The present work is organised as follows. First, the methodology is presented, starting with the proposed mathematical model. The main contributions of the model are also described, namely the integration of image-based biomarkers, the specific application of the model to neuroblastoma cancer, and the inclusion of the interaction between nutrients and cells as well as the cross-talk between cells and the extracellular matrix (ECM). Then, the boundary conditions and the numerical implementation are described. Finally, we show the application of the proposed methodology to simulate the tumour progression and validate with specific clinical cases. We go beyond clinical validation and present different alternative scenarios.

2 Materials and methods

The following section is organised into several key subsections, each contributing essential elements to our comprehensive approach. We start by detailing the constituents of our mathematical model and the transport of species. Following this, we present the governing equations for kinematics of tumour growth and remodelling. Another dedicated portion outlines our methodology for integrating image data into the model, ensuring patient-specific representations. The significance of boundary conditions is discussed separately, forming the foundational elements of our computational framework. A temporal multiscale approach is then outlined to simulate the dynamic interaction between nutrients, chemotherapy, and cells over time. The complex interplay between stroma and cells is explored through mechanical multiphase modelling in a dedicated section. Lastly, we provide insights into the numerical strategy guiding the implementation of our model, offering a comprehensive view of our computational framework.

2.1 Mathematical model of tumour growth and remodelling

Neuroblastoma tumours consists primarily of various types of cells and extracellular matrix. Of the many cell types, neuroblasts and non-tumoural cells are of primary interest, because they directly contribute to the mechanical properties of the tissue through the processes of proliferation, death or ECM production among others [19]. Extracellular matrix also has a principal role in the cell-microenvironmental cross-talk and it can promote the progression of the tumour. We here present a phenomenological model, which takes into account as detail as possible to better simulate the evolution of the tumour geometry. Our hypothesis proposes

that tumour evolution can be attributed to three distinct processes: growth, shrinkage, and remodelling. Localised growth is achieved through an increase in the number of cells, while localised shrinkage results either from cell death due to hypoxia or chemotherapy treatment or the degradation of ECM. Lastly, remodelling involves the reorganisation of existing constituents, leading to structural changes within the tumour. The two first processes result in a change of the mass of the constituents, and the later results in a change of the structure. To better address the processes of growth and remodelling, we apply the theory of mixtures, which states that every position of the tumour can be occupied simultaneously by multiple constituents.

2.1.1 Constituents

As a first approach, we consider a tumour consisting of three constituents ($M = 3$), namely the tumour cells—neuroblasts—, the non-tumoural cells and the ECM. The approach shown can be easily extended to any number of required constituents. Each population is defined by its density ρ^i, where $i = n, s, e$ stands for neuroblasts, non-tumoural cells, and ECM, and its change is driven by:

$$
\frac{\partial \rho^i}{\partial t} + \nabla \left(\rho^i \frac{\partial \mathbf{u}}{\partial t} \right)
$$
$$
= +k_p \left\langle \frac{(\rho^o - \rho^i_{crit})}{(\rho^o_{env} - \rho^i_{crit})} \right\rangle_+ - k_h \left\langle \frac{(\rho^i_{crit} - \rho^o)}{(\rho^o_{env} - \rho^i_{crit})} \right\rangle_+ \tag{1}
$$
$$
- k_c \mathcal{H}(\rho_c - \rho^c_{crit}) \mathcal{H}(\rho^n).
$$

From left to right, the terms in the left side of the equation correspond to the temporal rate of change of the i-th population density and the change in density due to volume growth. The ones in the right side corresponds to the net constituent production, the death due to hypoxia and the death due to the presence of treatment. The displacement of the tissue, $\mathbf{u}$, is caused by the growth of the tumour and by its deformation against the surrounding tissues and organs in location $\mathbf{x}$ at time t. Proliferation is driven by the presence of oxygen, where k_p defines this ratio of proliferation. The uptake of the different constituents can be due to hypoxia or to the presence of treatment, such as chemotherapy. Thus, k_h defines the ratio of cells that are dying by hypoxia and k_c defines the ratio of cells that are dying due to the presence of chemotherapy.

The Macaulay brackets $\langle \cdot \rangle_+$ indicate the positive value of the argument if the argument is positive, but zero if it is not. $\mathcal{H}$ denotes the Heaviside function. Both proliferation and death depend on the oxygen concentration ρ^o. It is assumed that there is a specific critical mass fraction of oxygen (ρ^i_{crit}) below which cells can no longer proliferate and begin to die. This critical mass fraction is believed to differ between cancer cells ($i = n$) and non-tumoural and ECM ($i = s, e$). Non-tumoural cells are thought to be regulated by physiological hypoxia, the lower level at which normal hypoxic responses are elicited. In contrast, tumour cells are regulated by pathological hypoxia, which is characterised by persistent poor oxygenation and disruption of normal homeostasis. The parameter ρ^o_{env} is the mass fraction of oxygen available in the environment [20]. This parameter can be defined as well as physoxia, the physiological oxygen level in peripheral tissues [21]. ρ^c represents the density of chemotherapy available in the tissue. It is modelled that only when that concentration reaches a critical value ρ^c_{crit} the tumoural cells start to die.

We do not model cell migration which is usually represented in a reaction diffusion equation through the diffusive term. Neuroblasts and non-tumoural cells do not exhibit a high migratory capacity [22, 23], so the diffusion term is neglected.

2.1.2 Species transport

Different species are transported all across the tumour. For the sake of simplicity, we have considered only oxygen and chemotherapy treatment. Each specie is defined by its concentration, ρ^j, where $j = o, c$ stands for oxygen and chemotherapy. We start from the standard form of the species transport equation:

$$
\frac{\partial \rho^j}{\partial t} + \nabla \left(\rho^j \frac{\partial \mathbf{u}}{\partial t} \right)
$$
$$
= +K^{Trans}(\rho^j_b - \rho^j) - \frac{A^j \rho^j}{k^j + \rho^j} \frac{\sum(\rho^i)}{\rho_c} - K^j_d \rho^j. \tag{2}
$$

On the left hand side, the temporal rate of change of the j-th population density and the change in density due to volume growth can be found. On the right hand side, the first term represents the species supply from the vascularisation. K^{Trans} is the extravasation parameter for the species along the tumour. This term also depends on ρ^j_b, the species concentration in blood. The following term corresponds to the j species consumption by the constituents. K^j_d is the decay coefficient of the j species, and A^j and k^j are the consumption coefficients for the j species, as defined in [7, 24]. More specifically, A^j is the maximum species consumption rate and k^j is the species concentration at which the total consumption term is one-half of the total consumption term. Notice that this consumption term is being multiplied by the cellularity, where ρ^i represents the different cell populations and ρ_c represents the tissue cells carrying capacity i.e., the maximum number of cells per unit of volume to prevent contact inhibition. It is assumed that only chemotherapy, $j = c$, can decay over time.
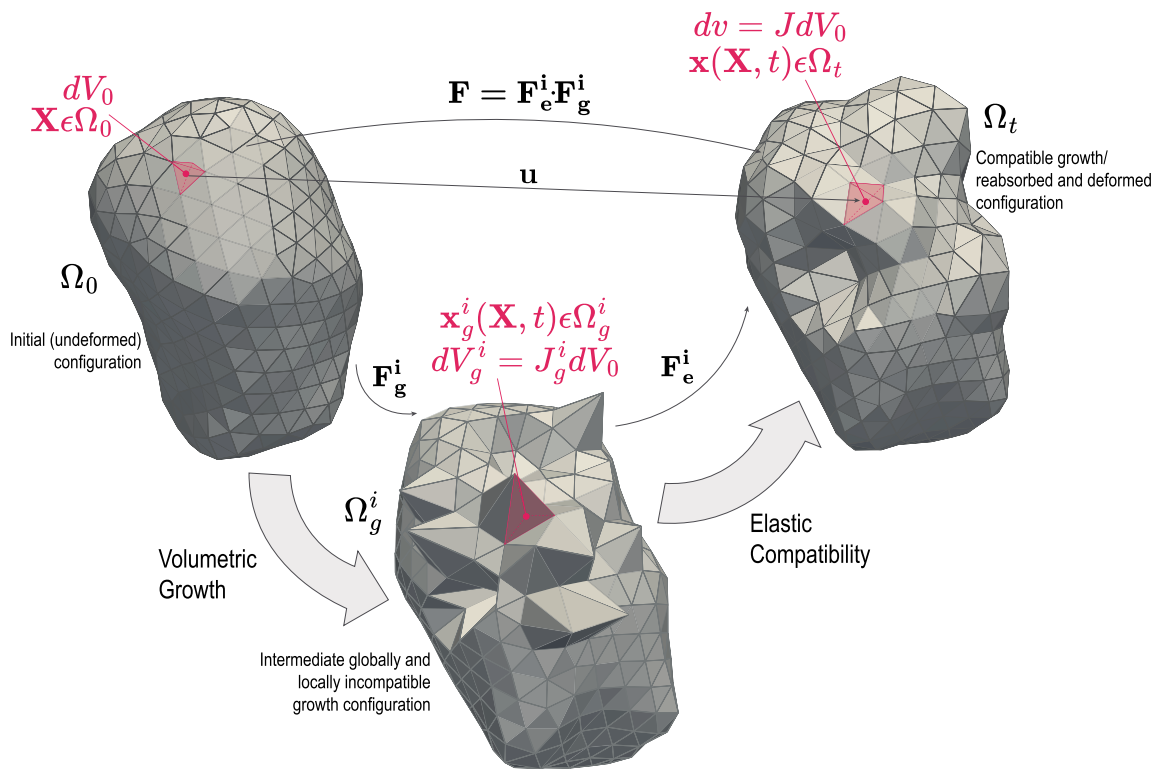
Fig. 1 Scheme of the motion from the original unstressed configuration Ω_0 to the current configuration Ω_t, through an incompatible configuration Ω_g^i. A multiplicative decomposition is applied to the deformation gradient $\mathbf{F}$ into a growth part $\mathbf{F}_g^i$ and an elastic part $\mathbf{F}_e^i$. In the kinematic growth theory, infinitesimal stress-free portions of the body growth independently via the transformation $\mathbf{F}_g^i$, which does not result in a compatible growth. An elastic assembly $\mathbf{F}_e^i$ yields to the configuration of interest, Ω_t

While it is widely recognised that diffusion influences how species spread within a tumour, in cases where the tissue is well-supplied with blood vessels (like neuroblastoma tumours), this diffusive effect might be hindered by active transport through the vascular network. Moreover, it is imperative to take into account the substantial computational expenses associated with the calculation of the diffusive process, which, based on our estimations, is approximately twenty times higher in cost. Consequently, due to the elevated degree of vascularisation in neuroblastoma tumours, we have decided to streamline the transport equation by excluding the diffusion term, thereby mitigating the computational burden associated with the model.

2.2 Kinematics of growth and remodelling

Let Ω be the neuroblastoma tumour embedded in the three-dimensional space (Fig. 1). A motion $\boldsymbol{\varphi} : \Omega_0 \to \Omega_t$ maps a material or reference configuration Ω_0 to a current configuration Ω_t via

$$\mathbf{x}(\mathbf{X}, t) = \boldsymbol{\varphi}(\mathbf{X}, t), \tag{3}$$

where $\mathbf{x}(\mathbf{X}, t)$ is the position at time t in the spatial configuration and $\mathbf{X}$ is the position in the material configuration. This movement $\mathbf{u}(X)$ can be described within the theory of nonlinear continuum mechanics as the deformation gradient,

$$\mathbf{F} = \frac{\partial \mathbf{x}}{\partial \mathbf{X}}, \tag{4}$$

as well as:

$$\mathbf{F} = \mathbf{I} + \frac{\partial \mathbf{u}}{\partial \mathbf{X}}, \tag{5}$$

where $\mathbf{I}$ is the identity matrix.

Constrained mixture models assume that a mechanical body consists in general of M different constituents. In this approach, we assume that there are three different constituents, namely tumour cells, the non-tumoural cells and the ECM. These constituents are characterised by their density $\rho^i = \rho^i(\mathbf{x}, t)$ at time t so that $\rho_0^i = \rho^i(\mathbf{x}(\mathbf{X}, 0), 0)$ is the density

at time $t = 0$, where $i = n, s, e$ stands for neuroblasts, non-tumoural cells and ECM. The initial and current mass of the i-th constituent are given by

$$dm_0^i = \rho_0^i(\mathbf{X})dV, \quad dm^i = \rho^i(\mathbf{x}, t)dv. \tag{6}$$

These different constituents share each differential volume element and they thus deform together, exhibiting the same deformation tensor $\mathbf{F}$. However, the single constituents may exhibit different deformations, reaching an incompatible configuration Ω_g^i.

The geometric deformation tensor can be decomposed as

$$\mathbf{F} = \mathbf{F}_e^i \cdot \mathbf{F}_g^i, \tag{7}$$

where $\mathbf{F}_e^i$ is the elastic deformation tensor and $\mathbf{F}_g^i$ the inelastic growth tensor. Thus, since mass is preserved along the path from Ω_g^i to Ω_t, the tensor $\mathbf{F}_e^i$ is not related to growth, but to the stress response of the material. However, $\mathbf{F}_g^i$ is the tensor directly connected to growth.

To reproduce tumour growth and remodelling, the change of mass needs to be considered for accurate stress–strain relations. Let be m^i the grown mass, v_g^i the volume in Ω_g^i and v the one in Ω_t. The densities of the grown mass with respect to the different configurations are given as

$$dm^i = \rho_g^i dv_g^i, \tag{8}$$

$$dm^i = \rho^i dv, \tag{9}$$

therefore, $\rho_g^i = \rho^i J_e^i$, where J_e^i indicates the volume ratio,

$$J_e^i = \det \mathbf{F}_e^i = \frac{dv}{dv_g^i}. \tag{10}$$

The growth deformation $\mathbf{F}_g^i$ can be modelled as the general form

$$\mathbf{F}_g^i = \vartheta_1^i \mathbf{v}_1 \otimes \mathbf{v}_1 + \vartheta_2^i \mathbf{v}_2 \otimes \mathbf{v}_2 + \vartheta_3^i \mathbf{v}_3 \otimes \mathbf{v}_3, \tag{11}$$

with ϑ_1^i, ϑ_2^i and ϑ_3^i the stretch ratios of every i-th constituent along the orthonormal vectors $\mathbf{v}_1$, $\mathbf{v}_2$ and $\mathbf{v}_3$, respectively.

Here, volume growth is considered isotropic, characterised by a single isotropic growth multiplier ϑ_g^i ($\vartheta_g^i = \vartheta_1^i = \vartheta_2^i = \vartheta_3^i$)

$$\mathbf{F}_g^i = \vartheta_g^i \mathbf{I}, \tag{12}$$

so that $J_g^i = (\vartheta_g^i)^3$ and $\mathbf{F}_g^i |_{\vartheta_g^i=1} = \mathbf{I}$.

We will say that growth takes place at $\mathbf{x}$ if $\rho_g^i > \rho_0^i$ and, conversely, that resorption takes place if $\rho_g^i < \rho_0^i$. We

assume that changes of mass production over the tissue carrying capacity (ρ_c) govern the inelastic deformation included via the factor $\vartheta_g^i(t)$:

$$\vartheta_g^i(t) = \begin{cases} 1 + k_d\left(\frac{\rho_g^i - \rho^i}{\rho^i}\right) & \text{if } \rho_g^i < \rho_0^i, \\ 1 + \frac{k_{v1}}{1 + k_{v2}\exp\left(\frac{-k_{v3}\rho_g^i}{\rho_c^i}\right)} & \text{if } \rho_g^i > \rho_0^i, \end{cases} \tag{13}$$

where k_{v1}, k_{v2}, k_{v3} are constants defining the growth rate and k_d governs the change of volume due to mass resorption.

Growth and remodelling happen in the time scale of days to months, whereas elastic deformations occur on the time scale of seconds. In this way, neglecting the body forces and inertia terms, the balance of linear momentum reads

$$div(\mathbf{P}(\mathbf{F})) = \mathbf{0}, \tag{14}$$

where $\mathbf{P}$ is the first Piola–Kirchhoff stress tensor.

Since we are dealing with a constrained mixture model, we therefore apply the continuum theory of mixtures to be able to model different mechanical properties and different natural configurations for the different constituents. Then, assuming that all the constituents ($i = n, s, e$) standing for neuroblasts, non-tumoural cells and ECM) are linear elastic we solve their mechanical behaviour by:

$$E^i(\mathbf{x}, t) = E_i \frac{\rho^i(\mathbf{x}, t)}{\rho_c^i}, \tag{15}$$

where $E^i(\mathbf{x}, t)$ stands for the homogenised elastic modulus in position $\mathbf{x}$ and time t, and E_i is the saturated elastic modulus for the different constituents.

2.3 Integrating image data to construct a patient-specific finite element-based simulation

The data available [26] for each of the cases consists of several MRI sequences taken at two different time points: the time of diagnosis and just after the end of the first treatment, separated by three months in time (Fig. 2). These sequences include a T2-weighted series, where the tumour was manually segmented by experienced radiologists and both Diffusion Weighted (DW) and Dynamic Contrast Enhanced (DCE) Magnetic Resonance (MR) sequences. From these segmentations, the 3D geometry of the tumour was reconstructed. To do this, we first extracted the contours of each of the segmented images and, using interpolation techniques, we obtained the point cloud that represents the 3D shape of the geometry surface. From this cloud,
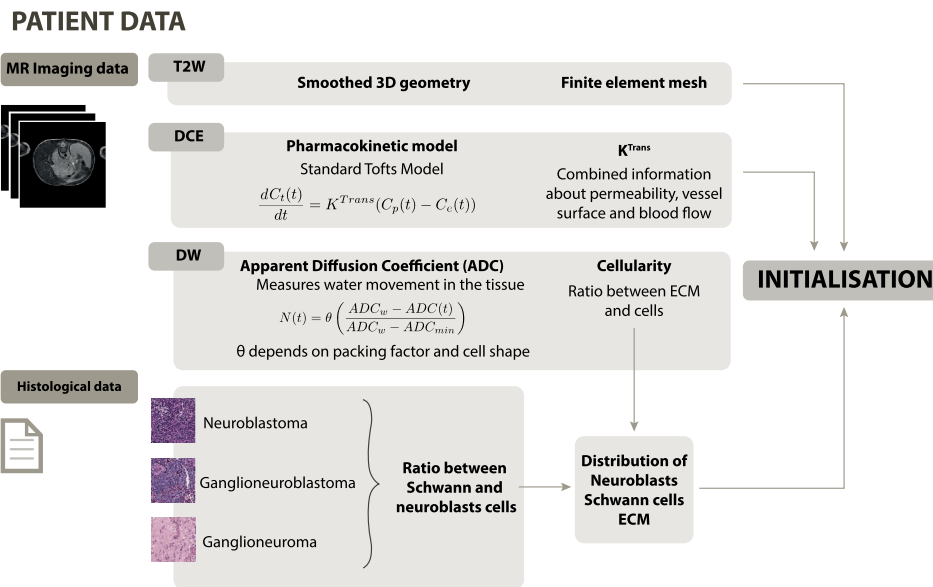
PATIENT DATA

Fig. 2 Processing patient data to initialise the biomechanical model. Magnetic resonance images are obtained from each patient. The tumour is segmented in the T2-weighted sequences, subsequently using these segmentations to reconstruct the 3D geometry. The reconstruction is carried out using the Python im2mesh library [25], resulting in a smooth FE mesh. Information about vascularisation is obtained from the DCE sequences. The Standard Tofts Model is used to obtain K^{Trans}, a parameter that informs about permeability, vessel surface, and blood flow. The DW sequences measure the ADC, a met-ric that quantifies the random movement of water within the tissue. This metric can be further used to approximate the ratio of cells in this tissue. This defines the cellularity, which is the ratio of volume occupied by cells and stroma. Each tumour has been biopsied, and the histology analysis allows classification into three different groups. Depending on the group, the neuroblasts content differs, enabling the estimation of the ratio between neuroblast cells and non-tumoural cells

we first reconstruct the surface and then the volumetric FE mesh of the tumour that will be used for the simulations. The Python library im2mesh [25] was used for this purpose. In addition to geometry, additional clinical data are necessary to initialise the model. In our case, these data consist of the spatial and time distribution of cellularity and vascularisation. To determine the former, we start from the ADC maps obtained from DW-MRI sequences. These maps measure the Brownian motion of water in the tissue, which is faster in the extracellular space than inside the cells. Assuming this correlation, the higher the cellularity ratio, the more restricted this motion will be (lowering ADC values). Considering that the diffusivity of water in a free medium is known, we can directly estimate the volume fraction of cellularity from the ADC maps following the method proposed by [27]. DCE sequences are employed to estimate the vascularisation of the tumour. This type of MR sequence consists on the injection of a contrast agent (CA) into the bloodstream, followed by the acquisition of images as this agent reaches the tumour. As a result we obtain a CA concentration vs time curve for each voxel in the tissue. We use then the Standard Tofts Model (STM) [28, 29] to fit its equation to these curves and obtain the STM parameters.

Among these parameters, we focus on the K^{Trans}, since it represents the extravasation rate of the CA, or equivalently, of the nutrients or the chemotherapy. In particular, this parameter measures the combination of blood flow, vessel permeability and vessel surface on each voxel, so it can be considered an estimate of the whole vascularisation. These cellularity and vascularisation maps were interpolated to the FE mesh previously generated, thus completing the generation of the necessary inputs for the model.

2.4 Boundary conditions

The surroundings of the tumour are fixed with springs in reference normal direction to mimic the stiffness of the surrounding tissue. The Young modulus assumed for the tissue carrying capacity is 50 kPa for a saturated cells-element and 500 kPa for a saturated ECM-element. The Poisson's ratio for both ECM and cells is set to 0.38 [33–36]. Since the histologies of both patients present important differences, Patient A is assumed to have initially 90% of neuroblasts and 10% of non-tumoural cells, whereas Patient B have a ratio of 30–70%. The parameters used in the simulation are listed in the Table 1.

Table 1 Parameters of the model

Symbol	Parameter	Value	Units	References
A^o	Oxygen uptake	2.55e1	pmol/s	[7]
k^o	Oxygen uptake	4.64e0	pmol	[7]
ρ_b^o	Oxygen blood concentration	3.62e3	pmol	[7]
A^c	Chemotherapy uptake	1.42e−1	µmol/s	[30]
k^c	Chemotherapy uptake	3.65e0	µmol	[30]
ρ_b^c	Chemotherapy blood concentration	1.00e1	µmol	[30]
K_d^c	Time of decay	4.80e1	h	Provided
ρ_c^n	Neuroblasts carrying capacity	1.00e5	cells/mm^3	[27, 31]
ρ_c^s	Healthy cells carrying capacity	1.00e5	cells/mm^3	[27, 31]
ρ_e	Tissue ECM carrying capacity	1.00e0	mg/mm^3	[32]
k_p	Cells proliferation rate	3.50e2	cells/d	[5]
k_h	Necrosis rate due to hypoxia	8.00e1	cells/d	Estimated
k_c	Necrosis rate due to chemotherapy	9.00e2	cells/d	Estimated
k_d	Shrinking rate	3.00e1	–	Estimated
k_{v1}	Min expansion rate	1.00e−1	–	Estimated
k_{v2}	Growth threshold	5.00e3	–	Estimated
k_{v3}	Net change rate	8.00e0	–	Estimated
ρ_{crit}^n	Threshold for neuroblasts proliferation	4.13e2	pmol	[21]
ρ_{crit}^s	Threshold for non-tumoural cells proliferation	7.75e2	pmol	[21]
ρ_{env}^o	Oxygen available at the environment	1.97e3	pmol	[21]
ρ_{crit}^c	Chemotherapy necrosis threshold	4.0e0	µmol	Estimated
E^{cell}	Young modulus of the cells	5.0e4	Pa	[33–36]
E^{ecm}	Young modulus of the ECM	5.0e5	Pa	[33–36]
ν	Poisson coefficient	0.38	–	[33–36]

2.5 Temporal multiscale simulation of oxygen, chemotherapy, and cells interaction

Cellular processes and the transport of molecules such as nutrients, oxygen and chemotherapy take place on very different time scales. Thus, while cells take days to proliferate or die, the arrival of these substances occurs in a scale of minutes. It is clear, therefore, that the two phenomena must be considered separately and subsequently the effects of both integrated. Consequently, in this work we have modelled the interaction between cells and these substances by means of a multiscale temporal algorithm. Given a time instant t, we begin by simulating the arrival of oxygen and chemotherapy until the equilibrium state of these substances is reached, which is achieved in a time Δt_d. With the distributions of these substances at equilibrium we proceed to simulate the cellular processes during a time Δt_b. Since the increment of time need to achieve equilibrium of species (Δt_d) is much smaller than the time where cell events occur (Δt_b), therefore $\Delta t_d \ll \Delta t_b$. Δt_d can be neglected and the equilibrium concentration of the substances can be considered constant throughout Δt_b. After the first time step, at instant ($t + 1$) we simulate again the arrival of substances, this time with the new cellularity values obtained from the calculation of the biomechanical model of the previous step (see Fig. 3).

2.6 Mechanical multiphase modelling of stroma-cell cross-talk

The importance of the interactions between the ECM and the cells are widely known, specially in tumour mechanics. To better incorporate this behaviour to the model, instead of following the theories of biological growth that model the tissue as a homogenised (single-constituent) solid continuum, both ECM and cells are separately modelled, but coupled on a strain approach. Therefore, based on the homogenised constrained mixture theory, it is assumed that, in each volume element, there exists a mixture of two structurally significant constituents: the cells and the stroma. Mass increments of each constituent are allowed to be deposited or removed within the body at each time. These increments possess different natural (stress-free) configurations and then deform together with the overall tissue (i.e., in a constrained manner). Thus, each solid portion of the mixture is assumed to be constrained, and each solid constituent has the same deformation as that of the solid-mixture at each point.
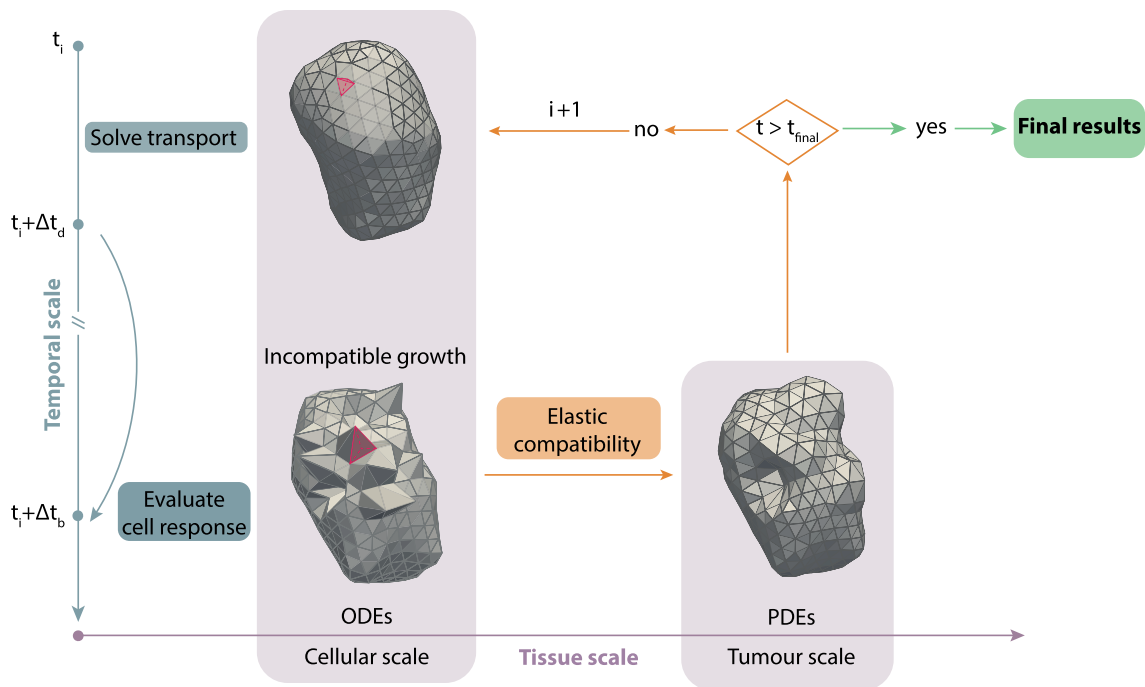
Fig. 3 Scheme of the phenomenological approach here presented. The simulation is initialised and starts with the cell metabolism model. First, the species of the model, namely oxygen and chemotherapy, distribution is calculated via a set of ordinary differential equations for a Δt_d. Since $\Delta t_d \ll \Delta t_b$, we assume the concentration to reach an stationary value which lasts until the end of the time step. Therefore, with this input, the mass of cells and ECM is updated. These increments exhibit different stress-free configurations, which lead to an incompatible growth of the whole tumour. Additionally, based on the new distribution of cells and ECM, different material properties are estimated for each element, based on the rule of mixtures. A mechanical analysis is performed to ensure that each solid constituent has the same displacement as the solid mixture and the whole body compatibility. Next, the iteration is considered complete, and the analysis is deemed finished if the final time is reached, or it continues if not. If it is necessary to proceed with the simulation, the mesh is updated every three steps, and the previous values are interpolated to the new FE mesh. Then, the convective term, which is uncoupled from the ODEs is updated and the cell metabolism model starts again from the previous geometry

Additionally, this approach also allows to model different material properties for each solid portion depending on the mixture present there.

2.7 Numerical implementation

The main goal of this work is to ascertain the evolution of a neuroblastoma tumour under different treatment scenarios. This biophysical target rewrites, in mathematical terms, in formulating a set of reaction–advection–diffusion equations, used to account the change of cells and ECM density. The proposed system is solved by the FE method with explicit time integration (Fig. 3). The mechanical analysis is performed separately from the biological one due to the assumption of incompatible growth. Therefore, the inelastic growth tensor is fully programmed in Python, and the elastic contribution is computed via the commercial Finite-Elements software Ansys®Academic Research Mechanical, Release 19.2. In order to simulate tumour growth or shrinkage, the thermoelastic expansion equations are used as an analogy that governs the volumetric changes in both contraction and expansion processes [37]. To simulate the tumour domain, we assume cellular contributions and ECM work in parallel, assuming a linear elastic material where the total stress of the tumour, under the finite strain assumption, is the sum of the cells and the ECM contributions. Strains are assumed to be equal in both parts of the tumour. To do so, the tumour domain is discretised in two overlapping conforming meshes sharing the nodes of the cells. Three-dimensional tetrahedral linear elements are produced by Gmsh [38] and updated each three time steps. Time-integration of the biological solver module is achieved using an explicit numerical scheme (forward Euler method), whereas the growth solver uses a full-implicit iterative scheme (Newton–Raphson). We performed a mesh refinement study and identified a mesh

with 63,775 linear tetrahedral elements for the patient B and 96,624 for A to yield a good tradeoff between computational efficiency and accuracy. By updating the geometry in each deformation, we adopt an updated Lagrangian approximation, whose formulation is also applied in the finite element analyses, to fulfil the hypothesis of finite deformations. In addition, enough small-time steps are simulated to assume linear elasticity in each step.

3 Results

Here, we applied the presented methodology to simulate the evolution of two different patient-specific neuroblastoma tumours, namely patient A and patient B. The section is structured as follows: first, the data available and the patients analysed are presented. Then, the model is validated using these data and the tumour outcome is evaluated. Finally, we explore further theoretical scenarios, where the chemotherapy treatment could be extended or a proangiogenic treatment could be administrated.

3.1 Clinical cases to study: patient-specific models

The tumour progression of two different patients is analysed. Both patients received the same treatment, although they were classified in different risk-groups.

Patient A, a male, was diagnosed with poorly differentiated neuroblastoma at the age of 16 months without presenting life-threatening symptoms. Tru-cut needle biopsy of the primary mass revealed low Mitosis-Karyorrhexis Index (MKI). Evaluation of bone marrow showed no metastases, and molecular studies showed no amplification of the MYCN gene. MRI imaging revealed that the abdominal mass was
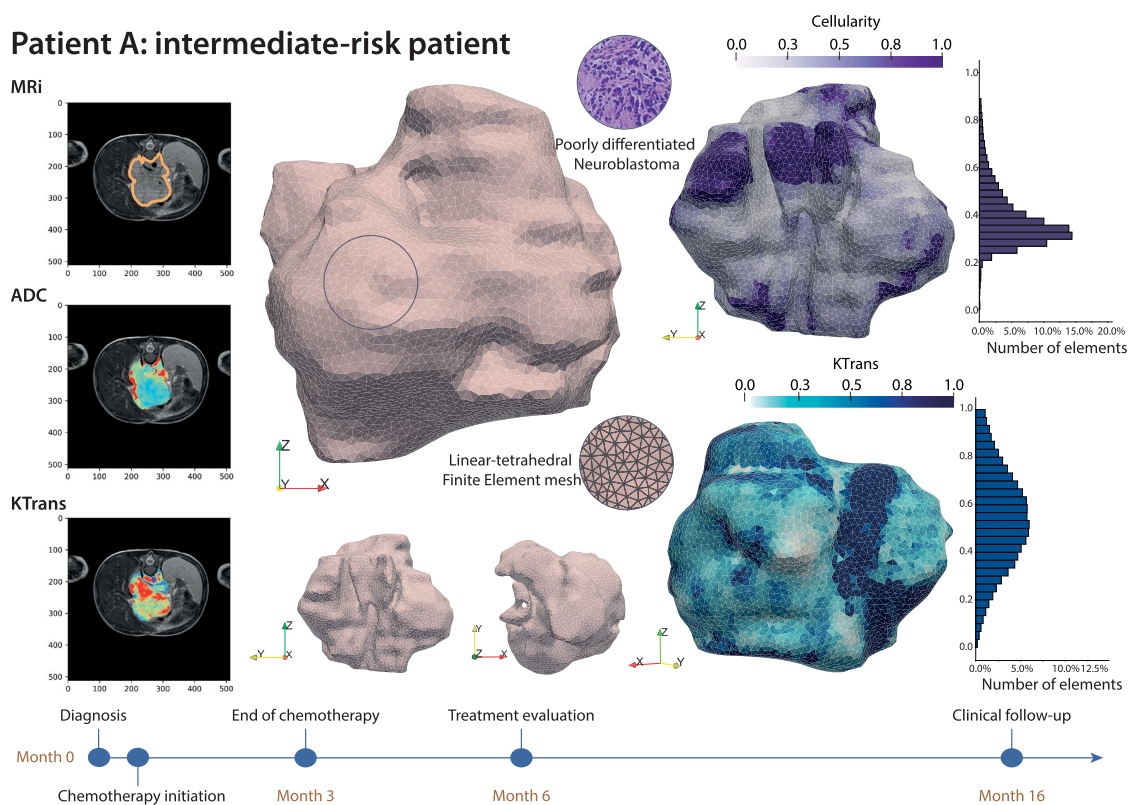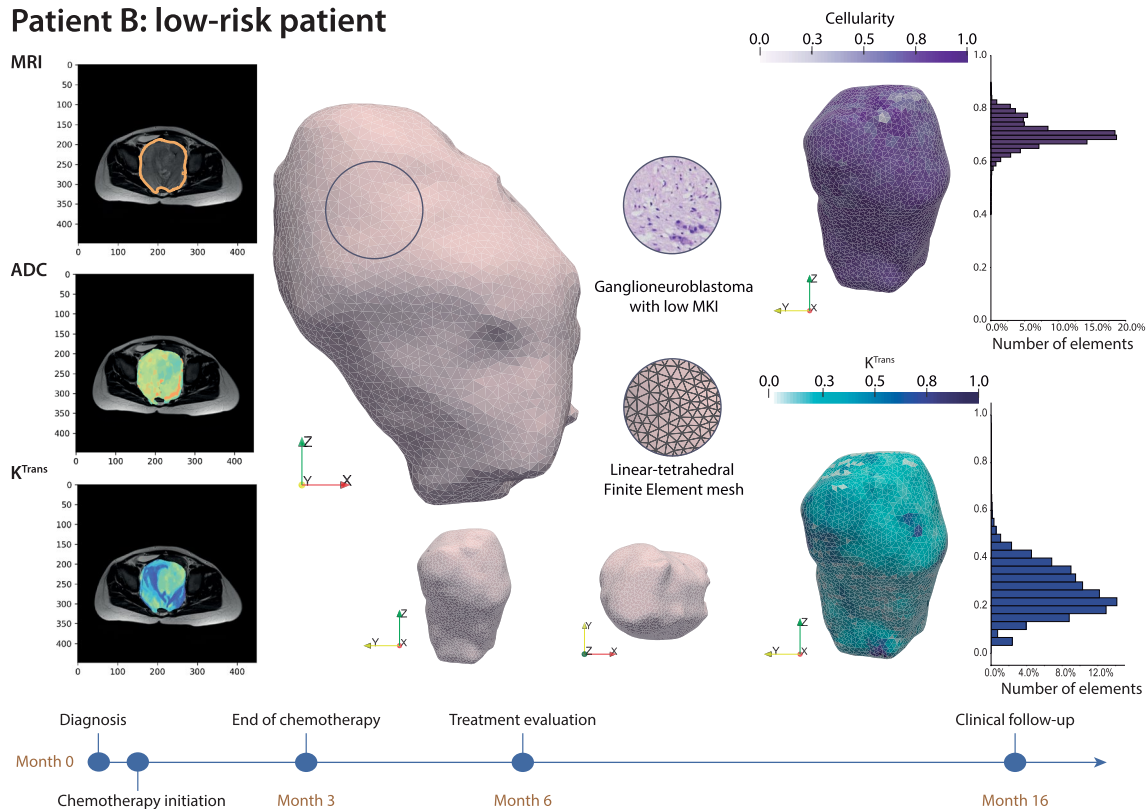

Fig. 4 Patient A. Left, clinical data available of the patient: MRI, ADC and K^{Trans}. The tumour is segmented over the MRI sequence. ADC maps inform about the tumour cellularity, whereas K^{Trans} reveal the vascularisation map. Centre, geometry of the tumour segmented from MRI sequences in three different orthogonal views. The geometry is discretised in a tetrahedral FE mesh. Right, cellularity distribution inside the tumour retrieved from ADC image. Frequency distribution of the cellularity in the whole volume of the tumour. K^{Trans} distribution in the tumour and its frequency distribution. The tumour presents low cellularity values and a more heterogeneous vascularisation. Bottom, time line of the diagnosis and treatment protocol followed

Fig. 5 Patient B. Left, clinical data available of the patient: MRI, ADC and K^{Trans}. The tumour is segmented over the MRI sequence. ADC maps inform about the tumour cellularity, whereas K^{Trans} reveal the vascularisation map. Centre, geometry of the tumour segmented from MRI sequences in three different orthogonal views. The geometry is discretised in a tetrahedral FE mesh. Right, cellularity distri-bution inside the tumour retrieved from ADC image. Frequency distribution of the cellularity in the whole volume of the tumour. K^{Trans} distribution in the tumour and its frequency distribution. The tumour presents higher cellularity values and a more homogenised vascularisation. Bottom, time line of the diagnosis and treatment protocol followed

encasing primary branches of the mesenteric artery, aorta, and vena cava. Based on these findings, the tumour was classified as intermediate risk according to the international neuroblastoma risk group classification. Chemotherapy was administered for 3 months, resulting in a partial response. Follow-up examinations showed no evidence of relapse or progression of the disease. The information available of this patient is summarised in Fig. 4.

Patient B, a female, was diagnosed with pelvic inter-mixed ganglioneuroblastoma at the age of 18 months, with no metastases present. At diagnosis, the patient presented bladder dysfunction. Tru-cut biopsy of the primary tumour revealed low MKI, and MYCN amplification was not observed in molecular studies. Evaluation of bone marrow metastasis yielded negative results. Image studies using MRI, CTE, and nuclear medicine did not reveal any defined risk factors. These findings led to the classification of the patient as belonging to the low risk group (international neuroblastoma risk group classification). Subsequently, the patient received chemotherapy treatment for three months,

resulting in a partial response, indicating a reduction in tumour size. Follow-up examinations showed no evidence of relapse or progression of malignancy. The information available of this patient is plotted in Fig. 5.

3.2 Predictive simulations and validation

According to the clinical report, both tumours have exhibited only partial responsiveness to chemotherapy. Nonetheless, upon conducting a volume analysis, it has emerged that the first tumour underwent a volumetric reduction of 90%, whereas the second tumour experienced a mere 20% reduction. Despite being reported a partial response in both cases, there has been a notable disparity in the response to chemotherapy exhibited by both tumours.

The mechanical model described in the material and methods section was applied to both cases, which are similar yet divergent, resulting in disparate outcomes.

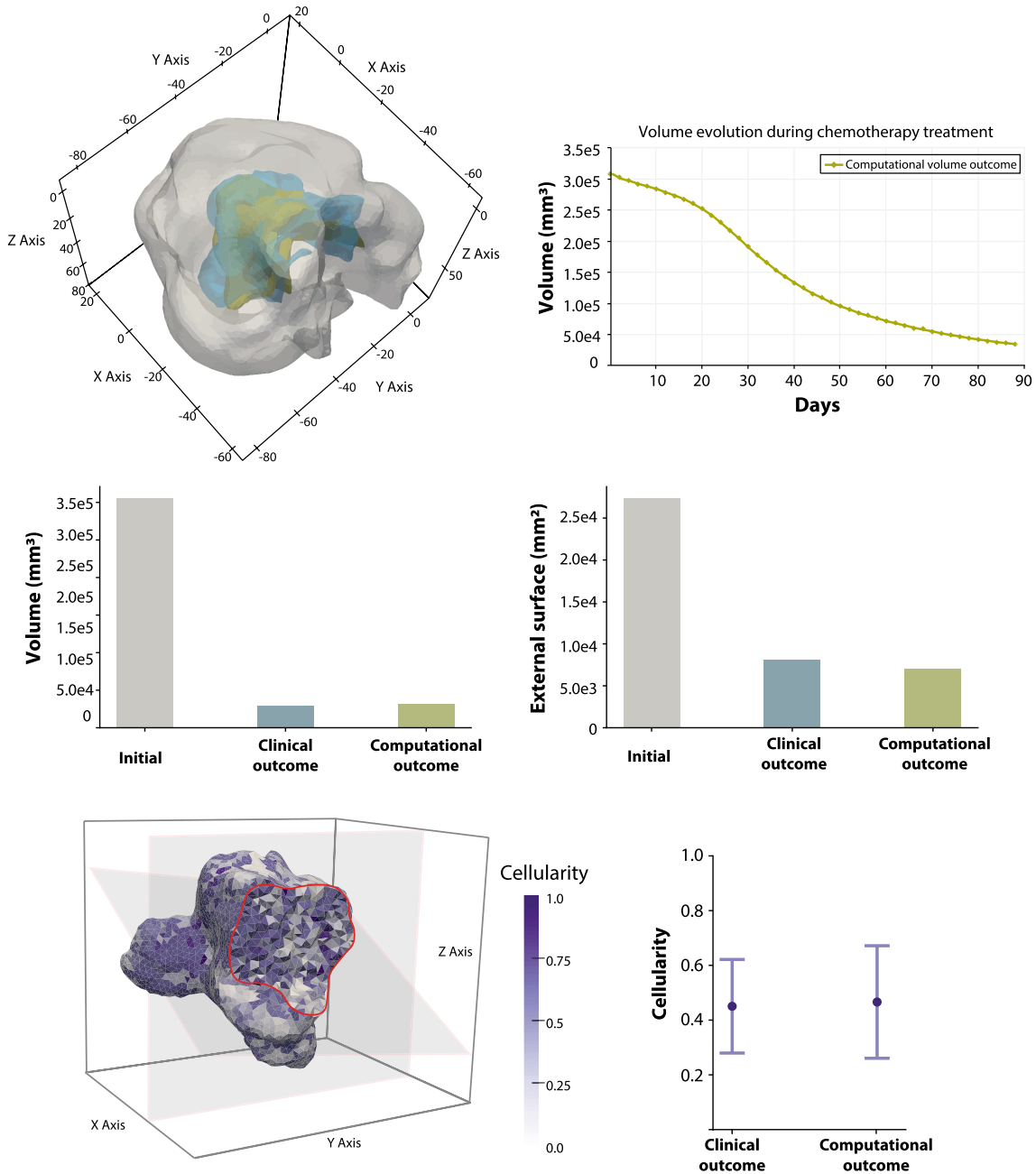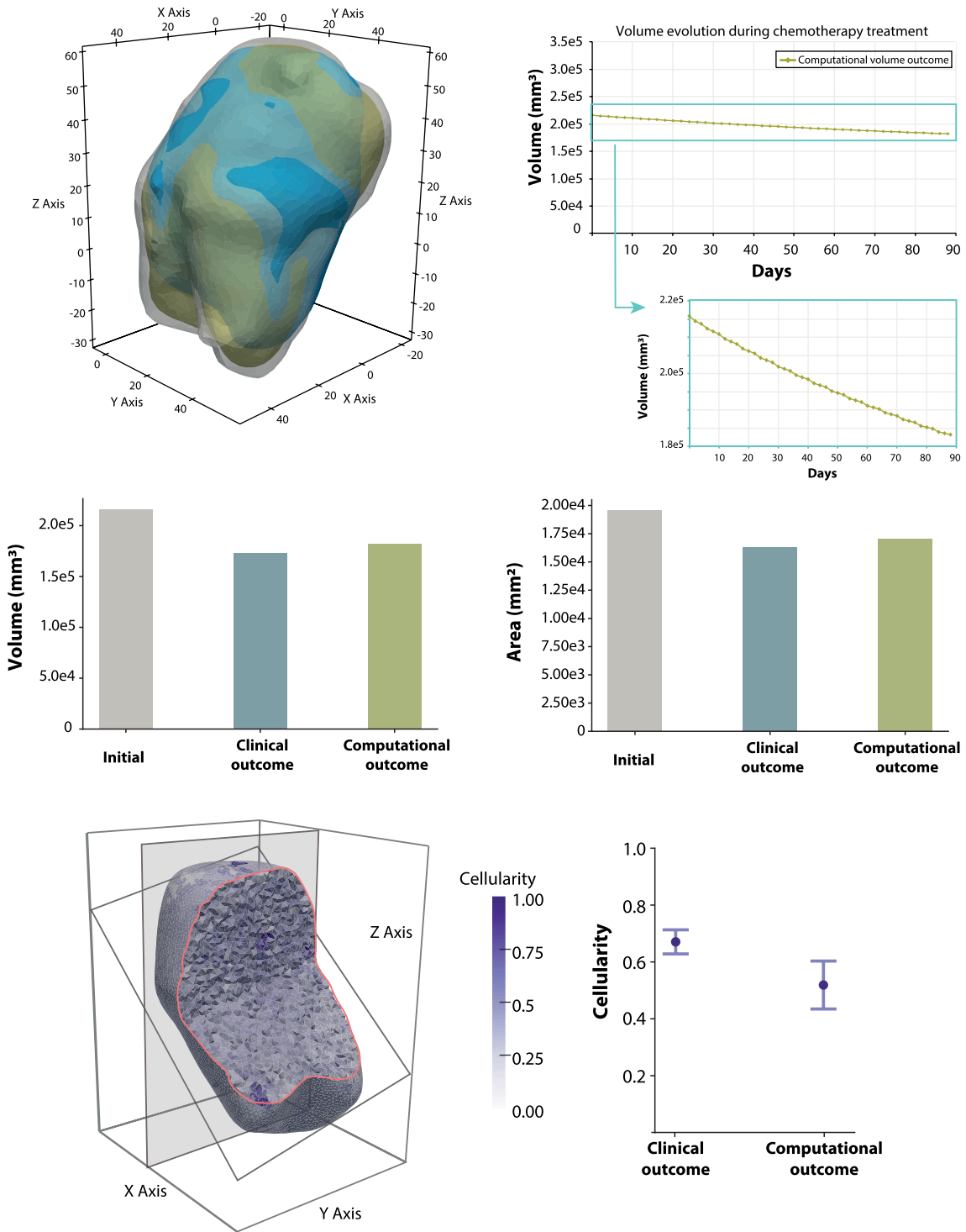# Patient A: intermediate-risk patient

Fig. 6 Patient A, numerical results in comparison with clinical outcome. Volume segmented at diagnosis is plotted in grey, whereas the segmentation of the tumour after the treatment is depicted in blue. In green, the computational outcome is plotted. At the bottom, the cellularity at the end of the simulation is plotted. Two transverse sections enable visualisation of the cellularity distribution within the tumour. Error bar plot show the differences between the clinical cellularity and the computational outcome. Circles depicts the mean of the values, whereas the bars depict the standard deviation (Colour figure online)

3.2.1 Patient A: intermediate-risk patient

Computational outcome shows a reduction in volume of 90.4%.

Patient A results are depicted in Fig. 6, illustrating that the clinical volume closely approximates the simulated outcome. Although the tumour shrinkage was gradual and reached a plateau value at the end, the final volume was slightly lower than the clinical value. The effectiveness of the computational model was demonstrated through bar plots comparing the volume and external surface of the tumour mass. Cellularity was evaluated in the computational

Patient B: low-risk patient

Fig. 7 Patient B, numerical results in comparison with clinical outcome. Volume segmented at diagnosis is plotted in grey, whereas the segmentation of the tumour after the treatment is depicted in blue. In green, the computational outcome is plotted. At the bottom, the cellularity at the end of the simulation is plotted. Two transverse sections enable visualisation of the cellularity distribution within the tumour. Error bar plot show the differences between the clinical cellularity and the computational outcome. Circles depicts the mean of the values, whereas the bars depict the standard deviation (Colour figure online)

simulation. Clusters of cells can be distinguished at the end of the simulation, with some clusters exhibiting extremely low cellularity, approaching zero, indicating that these regions consist primarily of extracellular matrix. However, other clusters still exhibit high cellularity, suggesting that chemotherapy treatment has not yet fully penetrated these areas. The cellularity assessed in the computational model shows more dispersion compared to that obtained from the clinical images.

3.2.2 Patient B: low-risk patient

Patient B was not responding to chemotherapy, the decrease of the volume observed in clinic was 20%, and the mechanical model predicts a shrinkage of 15.0%. The computational model also reproduces this behaviour by achieving a volume similar to that segmented at the end of treatment evaluation, along with a closely matching external surface value (Fig. 7). Although the tumour volume still shows a smooth trend, it does not reach a plateau value. The computational

model suggests that the tumour may continue to shrink if chemotherapy treatment is extended for a longer duration. In this case, the results indicate a slight reduction in cellularity from the initial value centred around 0.68, with the mean value obtained at the end of the simulation being 0.55. Comparing this data with the cellularity values obtained after chemotherapy treatment reveals a minimally higher value in the clinical outcome.

3.3 Further exploration of alternative scenarios

In this subsection, two distinct theoretical scenarios are analysed to broaden the scope of our investigation. Firstly, an exploration is conducted by extending the duration of chemotherapy treatment from 3 to 4 months. This investigation aims to assess the impact of prolonged treatment on the model's predictions and outcomes. Additionally, a separate scenario is examined, focusing on enhancing the level of vascularisation. This exploration serves to underscore the pivotal role of the vascular network in influencing the
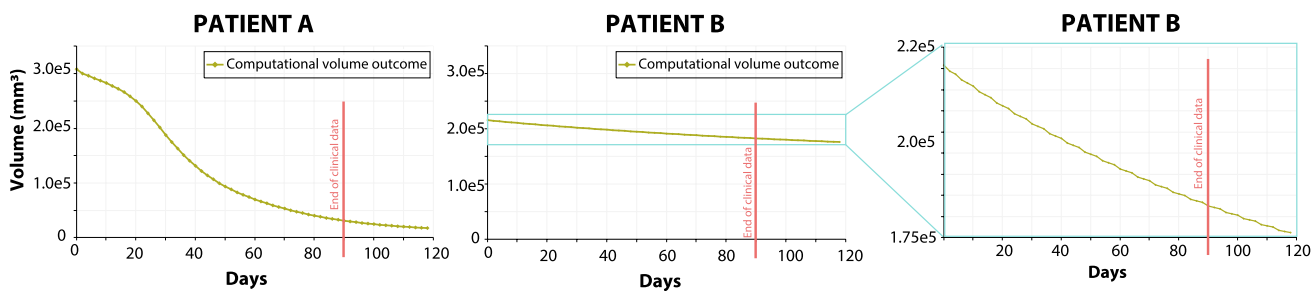

Fig. 8 Evolution of the volume over 4 months of treatment. In patient A, the rate of volume decrease is lower in the final month compared to the preceding 2 months. In patient B, the tumour continues to shrink after three months of chemotherapy, although at a slow rate
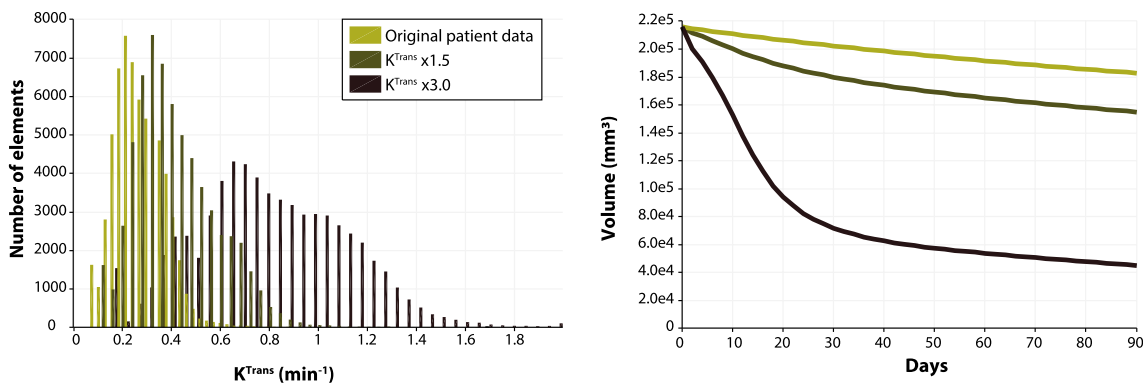

Fig. 9 Simulation of the scenario in which a proangiogenic treatment has been previously administered to the tumour. This proangiogenic effect has been modelled as an increase in the values of the K^{Trans} parameter. On the left, the histograms represent the different values of K^{Trans} at the beginning of the simulation. The original data is plotted in light green, and presents low vascularisation. In dark green, the

original data has been multiplied by 1.5. In brown, the original data is multiplied by 3.0. On the right, the evolution of the tumour volume is depicted. The light green one represents the original patient data. It can be observed that the more vascularised the tumour is, the more is the volume decreasing (Colour figure online)

efficacy of chemotherapy treatment. It is important to note that these results are purely theoretical in nature and have not undergone formal validation. These findings are intended to serve as initial insights into potential variations and alternative conditions, offering a preliminary exploration of the model's behaviour in scenarios beyond the clinically validated treatments. As such, caution should be exercised in interpreting these results, and further validation efforts are warranted to confirm the robustness and reliability of the model in these extended theoretical scenarios.

3.3.1 Extended chemotherapy treatment

We first present the outcome of the tumour if an extra month of chemotherapy would be administrated. In this scenario, the model predicts that the volume of the tumour would further decrease (Fig. 8). However, the decrease would only be an additional 5% for the patient A. In patient B, the volume is expected to decrease by a further 3%, which is not much compared to the overall 15% reduction achieved after three months of treatment. Therefore, as far as we can hypothesise, it would not be worth to administer an additional month of chemotherapy to get only a 5% reduction in volume, probably the best option would be to perform a surgery once the tumour is small enough. In this particular case, Patient B, the chemotherapy is failing to effectively reach the tumour, likely because of the inadequate blood supply indicated by K^{Trans}; therefore, radiotherapy might be a most suitable option [39].

3.3.2 Effects of a proangiogenic treatment

Since we have hypothesised that the tumour from patient B is not shrinking enough due to the lack of vascularisation, we then test the scenario where a proangiogenic treatment is previously administrated. To start with these new conditions, we have increased the K^{Trans} parameter in the whole tumour by multiplying it by 1.5 and 3 (Fig. 9, left). Therefore, we can simulate the scenario where the tumour is beforehand given a proangiogenic treatment. After that, chemotherapy would be administrated. The computational model then predicts, that the tumour is going to decrease its volume the more vascularised it is (Fig. 9, right).

4 Discussion

In this study, we present a predictive model for the response of tumours to chemotherapy, with the ultimate aim of testing the treatment before it is administered to the patient. Although there have been several studies on different forms of cancer [5, 6, 9, 10, 40], this particular work emphasises the importance of including the dynamics of tumour growth and the mechano-transport of oxygen and chemotherapy, while starting from MRI sequences to fully create a patient-specific model.

The model here proposed combines growth and remodelling theories with constrained mixture rules to better simulate the cross-talk between cells and tumour microenvironment [41–43]. While the ideal approach to modelling tumour evolution would be to incorporate detailed information about each constituent and their interactions, the current limitations in available clinical data mean that achieving fully realistic models remains a significant challenge. The formulation of the model allows to uncouple and simulate the mechanics of cells and the ECM separately, subsequently achieving compatibility. It is also more meaningful because it facilitates the incorporation of cellularity information, which varies significantly from patient to patient, as it has been shown in the data presented, and have a major impact on tumour progression and treatment response. Moreover, the mechanics of the surrounding tissue, and in particular the supportive ECM, have been found to be critical in shaping tumour growth and response. Mechanical aspects of the ECM such as tissue density and stiffness have been linked to cancer cell proliferation and motility [19, 44, 45], with strong correlations to the aggressiveness of the particular tumour.

Notably, the current assumption is that cell proliferation and death rates are not affected by current cell density. In order to uphold this hypothesis, we formulate the concentrations of the constituents to be representative of average values and ensure the absence of significant extreme value. Consequently, both the rates of proliferation and death will be dependent on the concentration of oxygen for each specific coordinate and time point.

In the present study, it is assumed that cellular proliferation and death may occur due to either hypoxia or chemotherapy treatment. Specifically, the model does not account for cellular migration, which simplifies the balance laws of the constituents. By replacing classical partial differential equations with ordinary differential equations, the computational efficiency of the model is greatly improved. This assumption is justified in neuroblastoma, as previous research has shown that cells in this cancer do not exhibit a high migratory phenotype [22, 23]. Furthermore, it is worth noting that cell processes occur on a different time scale than cellular proliferation or death, further supporting this decision.

The distribution of oxygen and chemotherapy within the tumour is obtained using a mass transport model. Two main hypothesis are considered to reduce the computational cost of this additional model. Firstly, the diffusive process of the species is considered negligible in comparison with the extravasation and consumption terms. Secondly, given the

significant difference in the temporal scales of cell processes and transport phenomena, both models are coupled in a temporal multiscale model.

The model here presented recovers the information of the vascularisation from DCE sequences. After applying the standard Tofts model [28], the parameter K^{Trans} is obtained for each point of the tumour at the initial time. This parameter informs on the permeability, vessel surface and blood flow. Thereafter, the vascularisation is considered static. Thus, this is considered as a limitation of the model that deserves further research but was out of the scope of this work.

In this manuscript, we demonstrate the efficacy of the model applied to two distinct patients. The patient-specific model was constructed using MRI sequences as well as DCE and DWI [26]. This data, along with the clinical report, was employed to establish the initial conditions of the mechanical model. It is important to note that the vascularisation and cellularity data are specific to each patient, while some parameters of the model are based on literature and others are estimated.

Both analyses simulated a 3-month chemotherapy treatment period and produced outcomes comparable to the actual results. The two patients were classified into two different risk groups—intermediate and low—and it is notable that the model is still able to predict both outcomes, even though chemotherapy resulted in significantly greater tumour shrinkage in one patient. Here, we demonstrate that the model is complex but straightforward enough to replicate this behaviour and offer a plausible explanation. Conversely, Patient A exhibits a higher degree of vascularisation. Following chemotherapy treatment, the tumour volume decreased by 90.4%, with areas of low cellularity indicating significant treatment efficacy. Interestingly, certain areas with higher cellularity were not affected by chemotherapy and remained isolated from the rest of the tumour. However, these regions may ultimately be eliminated through a process of cell competition. Such areas are localised within specific regions of the tumour and hold promise for future research into the mechanisms underlying tumour growth and treatment response. Patient B's low vascularisation indicates that angiogenesis has not been activated, which leads us to hypothesise that neither chemotherapy nor oxygen can reach the tumour cells and induce their death. We further explore the validated model and present alternative scenarios. However, it is worth highlighting that these additional results lack validation.

Additional exploration will be directed towards the development of a more complex model of chemotherapy, to be coupled with the presented model, accounting for detailed therapeutic mechanisms and pharmacodynamics.

The biomechanical model presented here does not have a large number of parameters. Most of them have been obtained from literature, while some had to be estimated. We can hypothesise that some parameters governing cell behaviour could be patient-specific, including the rates of proliferation and death, or how cells respond to chemotherapy. In order to gain more information in this sense, in vitro analyses could be conducted using patient-specific cells, the calibrated parameters measured experimentally could be translated to the macroscale model. Nevertheless, this has to be taken with caution since cells might not exhibit same behaviour in in vitro and in vivo conditions. Thus, as future work, the parameters of these macroscopic models can be fed by in vitro experiments, in order to build a full patient-specific model. In this field, microfluidic experiments are an excellent tool for understanding early tumour formation. Organoids experiments allow to reproduce the initial avascular steps in tumour development, as well as the vascular phase in bigger experimental set-ups. The combination of these experiments with physics-based models and the calibration of the former can feed the biological parameters of the macroscopic models [20, 46, 47].

The availability of data for paediatric malignancies is typically restricted, as minimising clinical testing for children is a priority. Additionally, in contrast to other malignancies such as breast or prostate cancer, the protocols in cancer in the young population are not fully defined. Therefore, modellers can obtain different data type acquisition for each patient, which makes the research process not straightforward. Consequently, patient-specific models have become increasingly necessary to compensate for the lack of available information. In this context, computational models serve as essential tools to aid in decision-making processes. It is important to note that developing models for paediatric populations is critical, as it can reduce the need for invasive and potentially harmful clinical tests. Despite the challenges associated with the limited availability of data, the presented computational model represents a promising step forward towards improving our understanding of paediatric cancers. In light of the above, it is essential to have a prognostic tool to help clinicians make decisions in childhood cancer to better tailor treatment, adjust dosage and timing, and minimise potential side effects. The mechanical model here presented is applied to paediatric neuroblastoma cancer, although it is sufficiently generalisable to be extended to other types of malignancy.

Declarations

References

1. Siegel RL, Miller KD, Fuchs HE, Jemal A (2022) Cancer statistics, 2022. CA: Cancer J Clin 72(1):7–33. https://doi.org/10.3322/caac.21708
2. W.H. Organization (2021) CureAll framework: WHO global initiative for childhood cancer: increasing access, advancing quality, saving lives
3. Swift CC, Eklund MJ, Kraveka JM, Alazraki AL (2018) Updates in diagnosis, management, and treatment of neuroblastoma. Radiographics 38(2):566–580. https://doi.org/10.1148/rg.2018170132
4. Schmelz K et al (2021) Spatial and temporal intratumour heterogeneity has potential consequences for single biopsy-based neuroblastoma treatment decisions. Nat Commun 12(1):6804. https://doi.org/10.1038/s41467-021-26870-z
5. Agosti A, Cattaneo C, Giverso C, Ambrosi D, Ciarletta P (2018) A computational framework for the personalized clinical treatment of glioblastoma multiforme. ZAMM-J Appl Math Mech/Zeitschrift für Angewandte Mathematik und Mechanik 98(12):2307–2327
6. Kremheller J, Vuong AT, Schrefler BA, Wall WA (2019) An approach for vascular tumor growth based on a hybrid embedded/homogenized treatment of the vasculature within a multiphase porous medium model. Int J Numer Methods Biomed Eng. https://doi.org/10.1002/cnm.3253
7. Mpekris F, Angeli S, Pirentis AP, Stylianopoulos T (2015) Stress-mediated progression of solid tumors: effect of mechanical stress on tissue oxygenation, cancer cell proliferation, and drug delivery. Biomech Model Mechanobiol 14(6):1391–1402. https://doi.org/10.1007/s10237-015-0682-0
8. Lorenzo G, Jarrett AM, Meyer CT, Quaranta V, Tyson DR, Yankeelov TE (2022) Identifying mechanisms driving the early response of triple negative breast cancer patients to neoadjuvant chemotherapy using a mechanistic model integrating in vitro and in vivo imaging data. https://doi.org/10.48550/arXiv.2212.04270. arXiv preprint. arXiv:2212.04270
9. Vavourakis V, Wijeratne PA, Shipley R, Loizidou M, Stylianopoulos T, Hawkes DJ (2017) A validated multiscale in-silico model for mechano-sensitive tumour angiogenesis and growth. PLoS Comput Biol 13(1):e1005259. https://doi.org/10.1371/journal.pcbi.1005259
10. Phillips CM, Lima EABF, Woodall RT, Brock A, Yankeelov TE (2020) A hybrid model of tumor growth and angiogenesis: in silico experiments. PLoS ONE 15(4):e0231137. Ed. by J.-L. Thomas. https://doi.org/10.1371/journal.pone.0231137
11. Xu J, Vilanova G, Gomez H (2020) Phase-field model of vascular tumor growth: three-dimensional geometry of the vascular network and integration with imaging data. Comput Methods Appl Mech Eng 359:112648. https://doi.org/10.1016/j.cma.2019.112648
12. Lampropoulos I, Charoupa M, Kavousanakis M (2022) Intratumor heterogeneity and its impact on cytotoxic therapy in a two-dimensional vascular tumor growth model. Chem Eng Sci 259:117792
13. Angeli S, Emblem KE, Due-Tonnessen P, Stylianopoulos T (2018) Towards patient-specific modeling of brain tumor growth and formation of secondary nodes guided by DTI-MRI. NeuroImage: Clin 20:664–673. https://doi.org/10.1016/j.nicl.2018.08.032
14. Fraldi M, Carotenuto AR (2018) Cells competition in tumor growth poroelasticity. J Mech Phys Solids 112:345–367. https://doi.org/10.1016/j.jmps.2017.12.015
15. Carotenuto AR, Cutolo A, Palumbo S, Fraldi M (2019) Growth and remodeling in highly stressed solid tumors. Meccanica 54(13):1941–1957. https://doi.org/10.1007/s11012-019-01057-5
16. Karolak A, Markov DA, McCawley LJ, Rejniak KA (2018) Towards personalized computational oncology: from spatial models of tumour spheroids, to organoids, to tissues. J R Soc Interface. https://doi.org/10.1098/rsif.2017.0703
17. Clarke MA, Fisher J (2020) Executable cancer models: successes and challenges. Nat Rev Cancer 20:343–354. https://doi.org/10.1038/s41568-020-0258-x
18. Cohn SL et al (2009) The International Neuroblastoma Risk Group (INRG) classification system: an INRG task force report. J Clin Oncol 27(2):289. https://doi.org/10.1200/JCO.2008.16.6785
19. Katira P, Bonnecaze RT, Zaman MH (2013) Modeling the mechanics of cancer: effect of changes in cellular and extra-cellular mechanical properties. Front Oncol 3:145. https://doi.org/10.3389/fonc.2013.00145
20. Hervas-Raluy S et al (2023) Tumour growth: an approach to calibrate parameters of a multiphase porous media model based on in vitro observations of Neuroblastoma spheroid growth in a hydrogel microenvironment. Comput Biol Med. https://doi.org/10.1016/j.compbiomed.2023.106895
21. McKeown SR (2014) Defining normoxia, physoxia and hypoxia in tumours—implications for treatment response. https://doi.org/10.1259/bjr.20130676
22. Abualsaud N, Caprio L, Galli S, Krawczyk E, Alamri L, Zhu S, Gallicano GI, Kitlinska J (2021) Neuropeptide Y/Y5 receptor pathway stimulates neuroblastoma cell motility through RhoA activation. Front Cell Dev Biol 8:627090. https://doi.org/10.3389/fcell.2020.627090
23. Pusch A et al (2010) CD44 and hyaluronan promote invasive growth of B35 neuroblastoma cells into the brain. Biochim Biophys Acta (BBA) Mol Cell Res 1803(2):261–274. https://doi.org/10.1016/j.bbamcr.2009.12.003. Includes Special Section on Formins
24. Casciari JJ, Sotirchos SV, Sutherland RM (1992) Variations in tumor cell growth rates and metabolism with oxygen concentration, glucose concentration, and extracellular pH. J Cell Physiol 151(2):386–394. https://doi.org/10.1002/jcp.1041510220

25. Sainz-DeMena D, García-Aznar JM, Pérez MÁ, Borau C (2022) Im2mesh: a Python library to reconstruct 3D meshes from scattered data and 2D segmentations, application to patient-specific neuroblastoma tumour image sequences. Appl Sci 12(22):11557. https://doi.org/10.3390/app122211557

26. Martí-Bonmatí L et al (2020) PRIMAGE project: predictive in silico multiscale analytics to support childhood cancer personalised evaluation empowered by imaging biomarkers. Eur Radiol Exp 4(1):1–11

27. Atuegwu NC, Arlinghaus LR, Li X, Chakravarthy AB, Abramson VG, Sanders ME, Yankeelov TE (2013) Parameterizing the logistic model of tumor growth by DW-MRI and DCE-MRI data to predict treatment response and changes in breast cancer cellularity during neoadjuvant chemotherapy. Transl Oncol 6(3):256–264. https://doi.org/10.1593/tlo.13130

28. Tofts PS, Kermode AG (1991) Measurement of the blood-brain barrier permeability and leakage space using dynamic MR imaging. 1. Fundamental concepts. Magn Reson Med 17(2):357–367. https://doi.org/10.1002/mrm.1910170208

29. Sainz-DeMena D, Ye W, Pérez MÁ, García-Aznar JM (2022) A finite element based optimization algorithm to include diffusion into the analysis of DCE-MRI. Eng Comput. https://doi.org/10.1007/s00366-022-01667-w

30. Kazmi N, Hossain MA, Phillips RM (2012) A hybrid cellular automaton model of solid tumor growth and bioreductive drug transport. IEEE/ACM Trans Comput Biol Bioinform 9(6):1595–1606. https://doi.org/10.1109/TCBB.2012.118

31. Weis JA, Miga MI, Arlinghaus LR, Li X, Chakravarthy AB, Abramson V, Farley J, Yankeelov TE (2013) A mechanically coupled reaction–diffusion model for predicting the response of breast tumors to neoadjuvant chemotherapy. Phys Med Biol 58:5851–5866. https://doi.org/10.1088/0031-9155/58/17/5851

32. Poon C (2022) Measuring the density and viscosity of culture media for optimized computational fluid dynamics analysis of in vitro devices. J Mech Behav Biomed Mater 126:105024. https://doi.org/10.1016/j.jmbbm.2021.105024

33. García-Gareta E, Pérez MÁ, García-Aznar JM (2022) Decellularization of tumours: a new frontier in tissue engineering. J Tissue Eng 13:20417314221091680. https://doi.org/10.1177/20417314221091682

34. Tsikritsis D, Richmond S, Stewart P, Elfick A, Downes A (2015) Label-free identification and characterization of living human primary and secondary tumour cells. Analyst 140(15):5162–5168. https://doi.org/10.1039/C5AN00851D

35. Hervas-Raluy S, Garcia-Aznar JM, Gomez-Benito MJ (2019) Modelling actin polymerization: the effect on confined cell migration. Biomech Model Mechanobiol 18(4):1177–1187. https://doi.org/10.1007/s10237-019-01136-2

36. Kwon S, Yang W, Moon D, Kim KS (2020) Comparison of cancer cell elasticity by cell type. J Cancer 11(18):5403. https://doi.org/10.7150/jca.45897

37. Vujošević L, Lubarda V (2002) Finite-strain thermoelasticity based on multiplicative decomposition of deformation gradient. Theor Appl Mech 28–29:379–399

38. Geuzaine C, Remacle J-F (2009) Gmsh: a 3-D finite element mesh generator with built-in pre-and post-processing facilities. Int J Numer Methods Eng 79(11):1309–1331

39. Juma VO, Sainz-DeMena D, Sánchez MT, García-Aznar JM (2023) Effects of tumour heterogeneous properties on modelling the transport of radiative particles. Int J Numer Methods Biomed Eng 39(11):e3760. https://doi.org/10.1002/cnm.3760

40. Wirthl B, Kremheller J, Schrefler BA, Wall WA (2020) Extension of a multiphase tumour growth model to study nanoparticle delivery to solid tumours. PLoS ONE 15(2):e0228443. https://doi.org/10.1371/journal.pone.0228443

41. Ambrosi D, Mollica F (2002) On the mechanics of a growing tumor. Int J Eng Sci 40(12):1297–1316. https://doi.org/10.1016/S0020-7225(02)00014-9

42. Ambrosi D, Ben Amar M, Cyron CJ, DeSimone A, Goriely A, Humphrey JD, Kuhl E (2019) Growth and remodelling of living tissues: perspectives, challenges and opportunities. J R Soc Interface 16(157):20190233. https://doi.org/10.1098/rsif.2019.0233

43. Rao I (2011) Modeling of growth and remodeling in soft biological tissues with multiple constituents. Mech Res Commun 38(1):24–28. https://doi.org/10.1016/j.mechrescom.2010.11.003

44. Tadeo I, Berbegall AP, Navarro S, Castel V, Noguera R (2017) A stiff extracellular matrix is associated with malignancy in peripheral neuroblastic tumors. Pediatr Blood Cancer. https://doi.org/10.1002/pbc.26449

45. Camacho-Gómez D, García-Aznar JM, Gómez-Benito MJ (2022) A 3D multi-agent-based model for lumen morphogenesis: the role of the biophysical properties of the extracellular matrix. Eng Comput 38(5):4135–4149. https://doi.org/10.1007/s00366-022-01654-1

46. Collis J, Connor AJ, Paczkowski M, Kannan P, Pitt-Francis J, Byrne HM, Hubbard ME (2017) Bayesian calibration, validation and uncertainty quantification for predictive modelling of tumour growth: a tutorial. Bull Math Biol 79(4):939–974. https://doi.org/10.1007/s11538-017-0258-5

47. Lima EABF, Faghihi D, Philley R, Yang J, Virostko J, Phillips CM, Yankeelov TE (2021) Bayesian calibration of a stochastic, multiscale agent-based model for predicting in vitro tumor growth. PLoS Comput Biol 17(11):e1008845. Ed. by S. Finley. https://doi.org/10.1371/journal.pcbi.1008845